

Design of illumination system using characterized illuminances for smartphone-based fundus camera

Seung-Jae Lee^{a,b}, Kyung-Mo Yang^b, Keun-Bum Lee^b, No-Cheol Park^{a,*}

^a Department of Mechanical Engineering, Yonsei University, 50 Yonsei-ro Seodaemun-gu, Seoul 03722, South Korea

^b Samsung Electronics Co., Ltd., 129 Samsung-ro, Yeongton-gu, Suwon-si, Gyeonggi-do 16677, South Korea

ARTICLE INFO

Keywords:

Smart-phone based fundus camera
Illumination system
Retinal illumination performance space
Retinal uniformity
Back-reflection suppression

ABSTRACT

Recently, smartphone-based fundus camera (SBFC) research has been actively conducted in response to the need to expand medical infrastructure in underdeveloped countries and the increased telemedicine since the COVID-19 pandemic. Compared to the conventional table-top system, SBFCs have technical challenges that make it difficult to guarantee uniform illumination and avoid back-reflection because of the design constraints of minimizing the form factor and cost. This paper proposes a novel illumination design methodology using characterized illuminance to obtain high-quality fundus images for SBFCs. Key performance indicators (KPIs), such as retinal uniformity, back-reflection suppression, and optical efficiency, were defined to evaluate the performance of the illumination system. Each KPI was calculated using optical simulation software based on Monte-Carlo ray tracing and mapped into a normalized three-dimensional coordinate, the retinal illumination performance space (RIPS). In RIPS, the KPIs are combined into a single parameter Δ_{RIPS} , which is the quantitative difference evaluated as the Euclidean distance between the ideal and actual design point. A compact SBFC illumination system with five design variables was presented to verify the proposed methodology. The final design values at the minimum Δ_{RIPS} were determined using the Taguchi method and response surface methodology. Finally, a working prototype was built, and fundus images were acquired by clinical testing under institutional review board approval. The fundus image had sufficient brightness and resolution to diagnose the lesion with a viewing angle of approximately 50° in one shot.

1. Introduction

A fundus camera is a non-invasive medical instrument used to obtain images of the rear of the eye, also known as the fundus, for diagnosis and monitoring of retinal diseases [1]. According to the World Report on Vision 2019 by the World Health Organization at least 2.2 billion people have vision impairment or blindness, of whom at least 1 billion have a vision impairment that could have been prevented or has yet to be addressed [2]. Visual impairment is a disease that is highly likely to be detected early. However, the lack of expensive diagnostic equipment in underdeveloped countries makes preventing the diseases difficult. Conventional table-top fundus cameras offer good-quality images but are bulky, office-based, technician-dependent, and costly [3]. Therefore, it is necessary to make fundus cameras cheaper and handier to expand medical access for visual disease diagnosis in third-world countries. In addition, the need for portable diagnostic equipment has increased as the demand for telemedicine has grown since the COVID-19 pandemic.

Over the past decade, research has been conducted on portable fundus cameras [4–9]. Among them, the smartphone-based fundus camera (SBFC) has the advantage of simplifying the structure of a diagnostic de-

vice because smartphones can utilize built-in cameras, display functions, high-performance computational processing, and wireless communication. Shanmugam et al. acquired fundus images with a system that attached a light-emitting diode (LED) and convex lens to a smartphone [10]. Wintergerst conducted a clinical test for retinopathy of prematurity by configuring a system equipped with a single lens on a smart device (iPod Touch 6th generation) and comparing the disease discrimination rate with the existing devices [11]. S. Thomas et al. constructed a low-cost system by combining a smartphone with a lens and proposed an algorithm to discriminate between diabetic retinopathy and age-related macular degeneration using convolutional neural networks [12]. However, the previously proposed devices make accurate image focusing inconvenient and necessitate several images because of the limited field of view (FOV). Furthermore, image quality was severely inferior to that of conventional table-top devices.

A typical fundus camera consists of imaging and illumination systems. The imaging system requires a wide FOV and high resolution to obtain high-quality fundus images [13]. Illumination systems require high illuminance uniformity and minimal back-reflection caused by reflections from the lens or corneal surface [14]. Köhler illumination is

* Corresponding author.

E-mail address: pnch@yonsei.ac.kr (N.-C. Park).

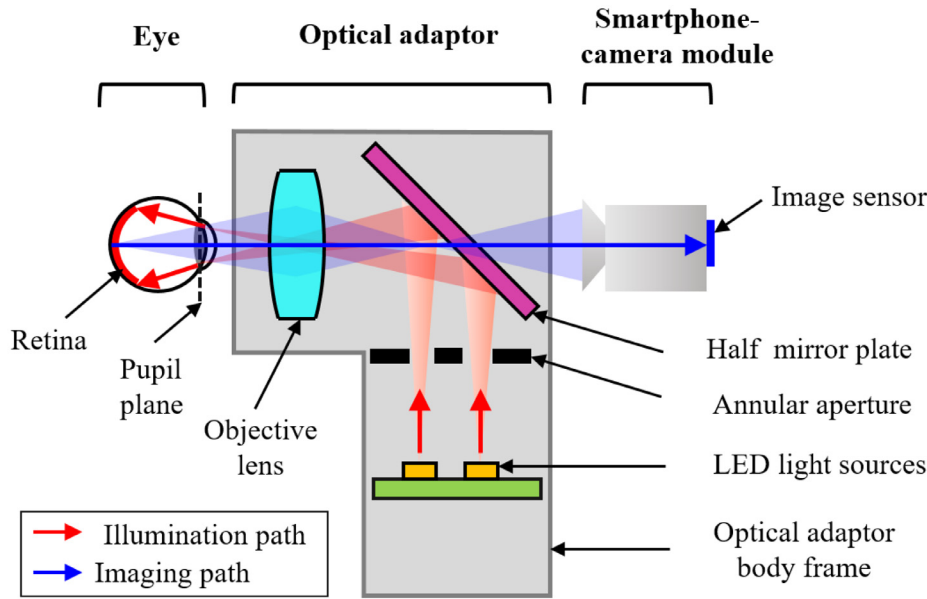


Fig. 1. Schematic diagram of the proposed SBFC.

sufficient to meet the requirements of the illumination system; however, it has limited application to SBFCs because of its bulky form factor and high cost. Hence, SBFCs face technical challenges in ensuring uniform illumination and avoiding back-reflection under design constraints of minimizing form factor and cost. An appropriate design methodology that can be applied in the illumination system design for SBFC is required to solve these problems.

DeHoog et al. defined performance indicators to be considered in fundus camera design and analyzed the performance trends according to the design variables [15]. However, the defined uniformity formula has a risk of decreasing accuracy in the case of multiple light sources. In addition, it is necessary to consider the back-reflection caused by lens surfaces. Ma et al. analyzed the optical path of back-reflection caused by lens surfaces using optical simulation and proposed a practical method to eliminate them [16]. However, there is a limitation to the trade-off of each performance in the optimization process because the mutual influence on significant performances, such as retinal uniformity and optical efficiency, is not considered.

In this study, to introduce the design methodology for the SBFC illumination system described above, key performance indicators (KPIs), such as retinal uniformity, back-reflection suppression, and optical efficiency, were proposed. The KPIs, for which it is difficult to find an analytic solution, are characterized using the illuminance data obtained through the Monte-Carlo raytracing simulation. Each KPI was mapped into a normalized three-dimensional coordinate, the retinal illumination performance space (RIPS). In RIPS, the KPIs are combined into a single parameter Δ_{RIPS} , which is the quantitative difference evaluated as the Euclidean distance between the ideal design point (IDP) and the actual design point (ADP). A compact SBFC illumination system with five design variables is presented to verify the proposed design methodology. The final design at the minimum Δ_{RIPS} was determined by applying the Taguchi method and response surface methodology. Finally, a working prototype was built, and fundus images were acquired by clinical testing under Institutional Review Board (IRB) approval.

2. Structure and simulation setup

2.1. Schematic of SBFC

A schematic of an SBFC is shown in Fig. 1. It is composed of a smartphone-camera module and an optical adaptor (OA). The OA's body frame contains the internal optical components that make up the illumination and imaging paths, block external light, and protect against

Table 1

Optical properties of the components in the optical simulation model.

Components	Optical Properties
Optical adaptor (OA)	Black polymer of 8% reflectance and $\sigma = 5^\circ$ Gaussian distribution
Objective lens (OL)	Transparent Polymer ($n_d = 1.53$) with anti-reflection (AR) coating
Half mirror plate (HMP)	Glass ($n_d = 1.50$) with AR and half mirror coating
Standard eye model	Based on Military Handbook 141 (US Defense Agency)
Dummy back cover	100% Absorption
Protecting cover	Transparent polymer ($n_d = 1.53$) with AR coating

mechanical disturbances from the external environment. The OA's internal optical components include LEDs, an annular aperture (AA), a half mirror plate (HMP), and an objective lens (OL). The light emitted from the LEDs travels along an illumination path. The AA controls the path of the light toward the 45° tilted HMP. The OL condenses the light reflected by the HMP and then forms a focus near the edge of the pupil. The light focused on the pupil diverges in the eye and illuminates the retina. The reflected light on the retina then travels through an imaging path. The reflected light returns to the OL through the eye and is directed to the image sensor via the OL and HMP.

2.2. Optical simulation setup

The optical simulation model of the SBFC shown in Fig. 2 was established based on the schematic shown in Fig. 1.

LightTools 9.1 from Synopsys, a commercial optical simulation software, was used to perform numerical ray tracing and 3D optical modeling manipulation. Optical components such as the LEDs, AA, OLs, HMP, standard eye model, and generic camera (GC), were generated in LightTools. Mechanical components, such as the OA body frame, smartphone dummy back cover, and protecting cover, were designed using CAD software, Siemens' NX 11.0, and exported to LightTools. The optical properties of the components, their surfaces, and their volumes are presented in Table 1.

The OA body frame is set as black polymer material with matte surfaces to minimize internal reflection. The scattering property of the black polymer surfaces is defined using a Gaussian distribution, given as

$$P(\theta) = P_0 e^{-\frac{1}{2} \left(\frac{\theta}{\sigma} \right)^2}, \quad (1)$$

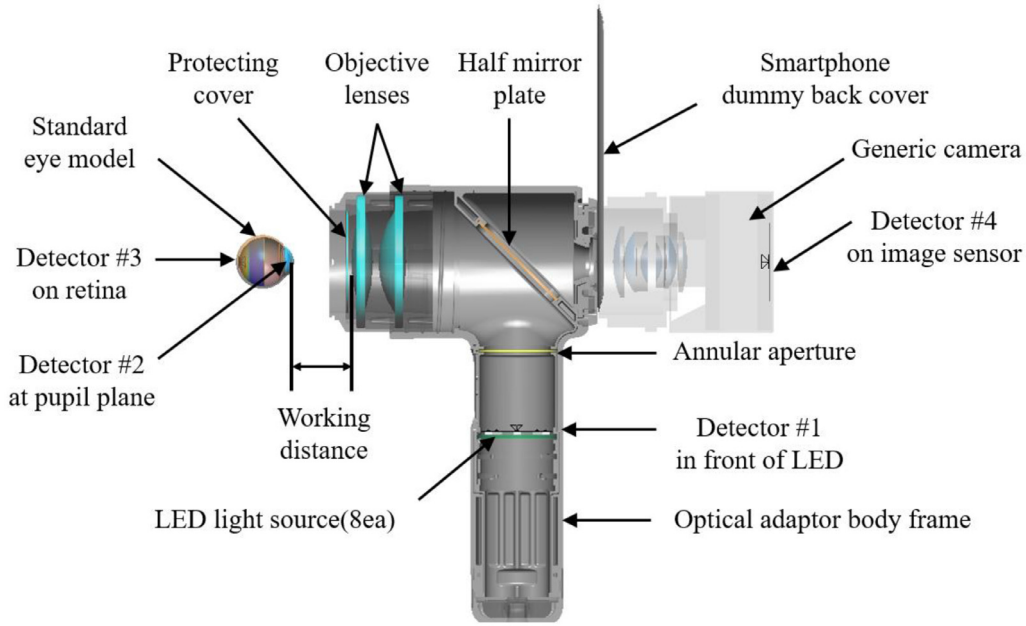


Fig. 2. Optical simulation model of the SBFC.

where θ is the angle of the ray incident on the surface. $P(\theta)$ and P_0 are the intensities in the θ and specular directions, respectively. σ is the standard deviation of the Gaussian distribution in degrees [17]. In this study, the surface reflectance of the black polymer material was 8%, and σ was set to 5° based on the measurement data for a specimen of the same material as the OA body frame, measured using a camera-based 3D hemispherical scattering measurement tool (Light Tec's Mini-diff V1). The AA was a 1.0 mm thick circular plate with an annulus hole, and its material and surface properties were specified to be the same as those of the OA body frame. The outer radius of AA was 18 mm.

The OL is a combination of two aspherical lenses made of a transparent polymer resin with a refractive index of 1.53, and the surfaces are treated with anti-reflection (AR) coating. The HMP is a 40 mm \times 40 mm \times 0.5 mm-thickness glass plate on which half mirror coating is applied to the surface facing the OL and AR coating on the opposite side. The human eye is an essential design factor because the image quality is affected by the optical properties of the retina, cornea, etc. In the optical model, a standard eye model was applied from the LightTools Software Library [18], which is based on Military Handbook 141 published by the U.S. Department of Defense [19]. The pupil diameter was specified with a maximum diameter of 7.5 mm to simulate the eye being dilated [20]. The working distance (WD) is the distance between the vertex of the cornea and lens vertex of the inspector. If WD is not guaranteed, the lens part of the device may collide with the subject's eye. Hence, an appropriate WD should be considered a design factor, and it was set to 26 mm. A downsized Single-Lens Reflex camera model, GC, provided by LightTools, was included in the optical model instead of a mobile phone camera. This is because the primary purpose of the optical model is to optimize the illumination path, including the standard eye model, and the optical model of a mobile phone camera is typically confidential.

Eight LEDs were arranged at equal intervals in a circle on the PCB. Each LED package has dimensions of 3.4 mm \times 3.2 mm \times 1.4 mm and has a luminous intensity of 70 cd with Lambertian angle distribution. The dimensions of the optical simulation model components are summarized in Table 2.

The rays emitted from the LEDs were collected in five meshed 2D illuminance detectors to analyze the optical performance of the optical model of the SBFC. As shown in Fig. 2, the first detector was placed at the LEDs and the second at the AA in the OA. The third and fourth detectors

Table 2

Dimensions of the optical simulation model components.

Items	Dimensions
Annular aperture (AA)	18 mm outer radius and 1.0 mm thickness
Half mirror plate (HMP)	40 mm \times 40 mm \times 0.5 mm thickness
Pupil diameter (PD)	7.5 mm
Working distance (WD)	26 mm
LED package	3.4 mm \times 3.2 mm \times 1.4 mm

Table 3

The size and mesh dimensions of the illuminance detectors.

No.	Location	Detector Size (mm)	Mesh Dimensions (bins)
1	LEDs	32.0 \times 32.0	51 \times 51
2	AA	32.0 \times 32.0	51 \times 51
3	Pupil	10.0 \times 10.0	101 \times 101
4	Retina	22.2 \times 22.2	51 \times 51
5	Image sensor	30.0 \times 30.0	75 \times 75

were located on the pupil and retina of the eye, respectively. The fifth detector is on the image sensor of the GC. The size and mesh dimensions of the illuminance detectors are listed in Table 3. The illuminance of each detector is calculated using the Monte-Carlo ray tracing method.

3. Definition of KPIs

The KPIs are introduced in this Section to evaluate the performance of the SBFC illumination system. KPIs are defined to quantify the significant optical performance of the illumination systems for SBFC and are calculated by characterizing the illuminance obtained by optical simulations. In this study, KPIs included retinal uniformity, back-reflection suppression, and optical efficiency. The KPIs are normalized to have values between zero and one, with higher values indicating better illuminance performance.

3.1. Retinal uniformity

Retinal uniformity is a performance indicator of retinal surface uniformity. It is defined as the product of the min-max ratio and the smoothness of the distribution, and both are characterized by the illuminance from the detector on the retina. First, the min-max ratio U_r is determined

by dividing the minimum illuminance of the retina by the maximum as follows:

$$U_r = \frac{\min[E_r(x, y)]}{\max[E_r(x, y)]}, \quad (2)$$

$E_r(x, y)$ represents the illuminance at a specific location, indicated by x, y , within 75% of the radius defined from the center to the edge of the illumination area. The target illumination area is synchronized with the camera's target FOV to aid in diagnosing lesions on the macula and optic disk. The minimum recommended FOV for fundus cameras, according to ISO 10,940:2009, is 30° [21], and the FOV of commercialized devices generally ranges from 40 to 60° [3]. In this paper, a lower limit of target FOV is assumed to be 40°. Therefore, in order to ensure uniformity within the minimum recommended FOV of 30° (which is 75% of 40°), illuminances within the 75% in the radial direction of the illuminated area were taken into consideration. Second, the smoothness of the distribution is defined by considering the perceived uniformity. The perceived uniformity varies depending on the spatial distribution, despite the similar min-max ratio of illuminance [22]. According to a previous study in the display field, perceived non-uniformity can be quantified using the rate of change in the brightness deviation on the screen [23]. Therefore, the non-uniformity of $E_r(x, y)$ can be described by the rate of change of the difference between adjacent illuminances. The representative value of the non-uniformity for the entire area is defined as the maximum absolute change rate of the difference between $E_r(x, y)$. This is because image defects at a specific location affect the overall image quality, and defining non-uniformity as a sum or average value cannot effectively reflect locally occurring defects. Therefore, the non-uniformity N_U of $E_r(x, y)$ is defined based on the second derivative of $E_r(x, y)$ as

$$N_U = \max[|E_r''(x, y)|], \quad (3)$$

where $E_r''(x, y)$ is the second derivative of $E_r(x, y)$ in spatial coordinates, and is approximated by the second-order forward finite difference method in the calculation process. Subsequently, N_U is normalized by dividing the mean of $E_r(x, y)$ because the effect of N_U depends on the background illuminance level of the retina. The normalized non-uniformity N_{Ur} was calculated as follows:

$$N_{Ur} = \frac{N_U}{\text{mean}[E_r(x, y)]}. \quad (4)$$

As N_{Ur} increases, the performance of the illumination system deteriorates. Therefore, to evaluate the performance of the illumination system, the smoothness of the distribution U_s is defined as

$$U_s = \frac{1}{1 + N_{Ur}}. \quad (5)$$

U_s indicates how steeply the illuminance change occurs in the adjacent area within the illuminated area, and the value range is between zero and one. Moreover, the closer it is to one, the more uniform the illuminance.

The min-max ratio U_r is representative of the uniformity of the overall illuminance distribution over the entire illuminated area, while U_s is the local distribution change at any position. Therefore, considering these two factors, the retinal uniformity R_U , a KPI representing the uniformity of illumination on the retina, is defined as

$$R_U = U_r U_s. \quad (6)$$

U_r and U_s have values between zero and one; hence, R_U has values between zero and one.

In contrast, in a previous study [8], the conventional uniformity formula is defined as

$$U = 1 - \frac{|E_c - E_{85\%}|}{E_{\max}}, \quad (7)$$

where U represents the illuminance uniformity on the retina, E_c is the illuminance at the center of the illumination area, and $E_{85\%}$ is the illuminance at 85% of the radial direction from the center of the illumination area. E_{\max} is the maximum illuminance in the illuminated area.

U and R_U differ in their consideration of spatial distributions that affect the perceived uniformity. Fig. 3 shows 2D illuminance distribution and x -direction slice charts for four different cases to compare between the conventional U and the proposed R_U . Fig. 3(a) represents the reference, which can be regarded as the practically highest value for uniformity. Fig. 3(b) shows a practically acceptable distribution with illuminance gradually decreasing towards the edges. Fig. 3(c) and (d) demonstrate probable cases of a circular arrangement of multiple light sources such as LEDs. In Fig. 3(a) and (b), the values U are 0.997 and 0.648, and the corresponding values of R_U are 0.779 and 0.598, respectively. The decrease in both U and R_U in Fig. 3(b) compared to Fig. 3(a) is consistent with perceived uniformity. For Fig. 3(c) and (d), where multiple light sources are used, the values of U are 0.808 and 0.682, while the values of R_U are 0.498 and 0.215, respectively. As observed in Fig. 3(c) and (d), there is a significant increase in illuminance difference between the adjacent areas compared to Fig. 3(a) and (b), indicating lower perceived uniformity. However, U of Fig. 3(c) and (d) are greater than that of Fig. 3(b), contradicting the perceived uniformity. In contrast, R_U provides a reliable reflection of the perceived uniformity. These findings suggest that R_U is more appropriate in situations with multiple light sources, where conventional U may not yield accurate uniformity. Traditional fundus cameras usually incorporate a single tungsten light source, making the conventional method problem-free. However, when multiple light sources are utilized, a more accurate formula for uniformity evaluation is necessary, and R_U is more suitable in such situations.

3.2. Back-reflection suppression

Back-reflection suppression indicates the extent to which the back-reflection prevents in the image. Back-reflection must be minimized and handled carefully during the design stage because it decreases the quality of the fundus image. Back-reflection in a fundus camera is mainly caused by two factors. The first is the reflection from the emitting area of the light source on the corneal surface. Since the cornea has significantly greater spectral reflectivity than the retina in the visible light band [24], the light reflected by the cornea appears as a hotspot in the image. The second is an unintentional bright light focused on the image sensor after being reflected on the lens surface or optical components.

To quantify back-reflection, the illumination ratio at the pupil and back-reflection contrast on the image sensor was introduced. To reduce corneal back-reflection, it is necessary to prevent as much incident light as possible from passing through the center of the pupil. The illumination ratio B_{pr} at the pupil, which represents the ratio of the peak illuminances of the center area to that of the entire pupil, is defined as

$$B_{pr} = \frac{\text{Max}[E_{p50\%}(x, y)]}{\text{Max}[E_p(x, y)]}, \quad (8)$$

where $E_p(x, y)$ is the illuminance of the entire area of the pupil and $E_{p50\%}(x, y)$ is the illuminance in the region within 50% of the radial direction of the entire pupil. A higher B_{pr} indicates that more light passes through the central area of the pupil. Luminance contrast is generally defined as the luminance ratio between a target and its background [25]. Similarly, the luminance contrast for the back-reflection was determined based on the luminance relationship between the back-reflection and the background on the image sensor. Here, the luminance ratio can be replaced with the illuminance ratio obtained from the image sensor detector in GC because it is known that luminance is proportional to the camera's image sensor pixel values, corresponding to illuminance [26]. Therefore, the back-reflection contrast B_{cr} is defined as

$$B_{cr} = \frac{\text{Max}[E_{br}(x, y)]}{\text{Mean}[E_{bg}(x, y)]}, \quad (9)$$

where $E_{br}(x, y)$ and $E_{bg}(x, y)$ are the illuminances of the back-reflection and background on the image sensor, respectively. $\text{Max}[E_{br}(x, y)]$ is calculated from the illuminance on the image sensor by setting only

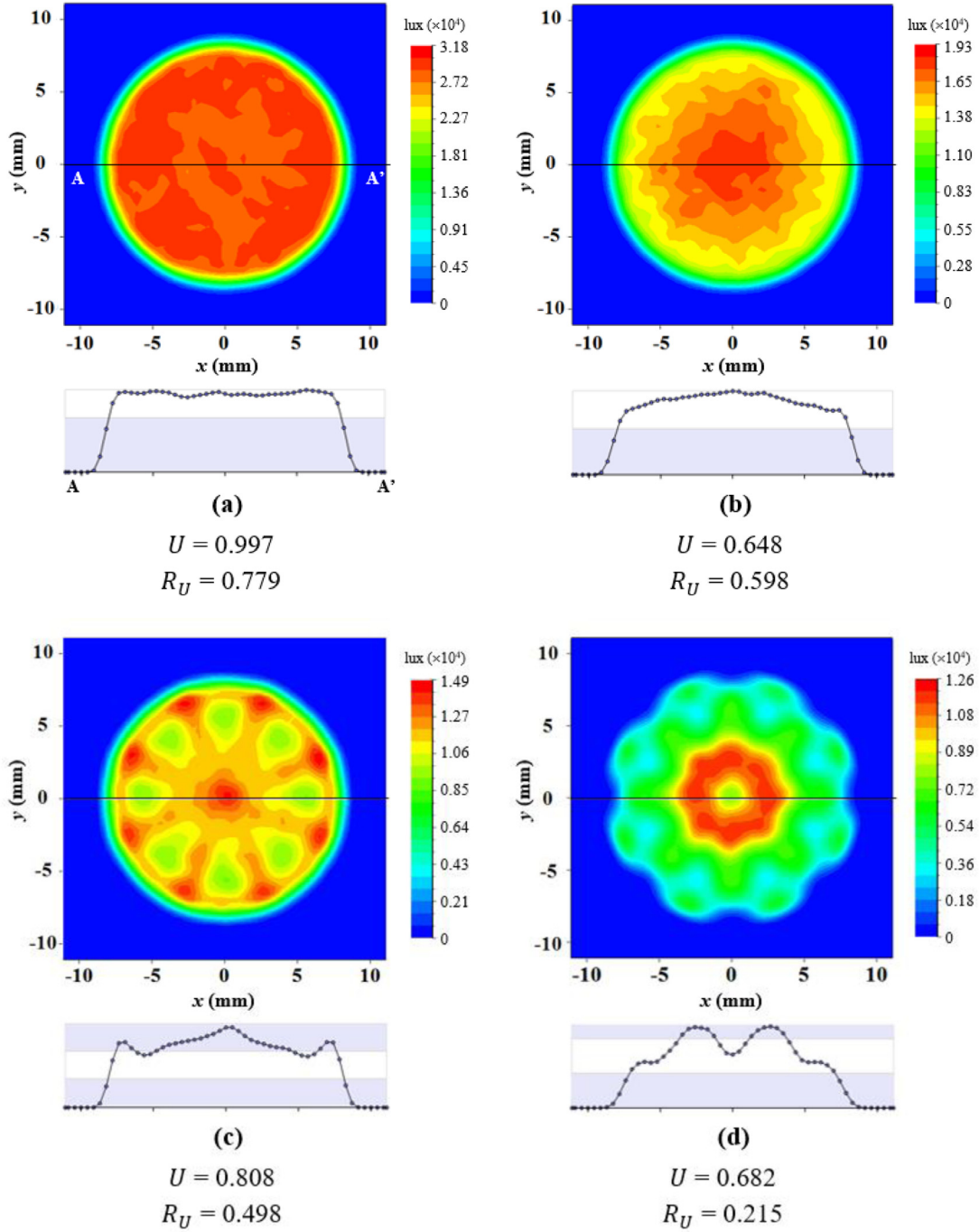


Fig. 3. 2D illuminance distribution and x-direction slice charts for four different cases to compare between the conventional U and the proposed R_U ; (a) reference, (b) practically acceptable distribution, (c) multiple light sources I: Eight LEDs in a circular array with 12 mm radius, (d) multiple light sources II: Eight LEDs in a circular array with 9 mm radius.

the retina surface as a complete absorber in the optical simulation. If the retina reflects no rays, only the back-reflection portion, $E_{br}(x, y)$, remains on the image sensor with $E_{bg}(x, y) = 0$. $\text{Mean}[E_{bg}(x, y)]$ is obtained by averaging the illuminance under conditions in which the retina is set typically, and the cornea and all lens surfaces are set to complete transmission. Only background portion is extracted through this process. As B_{pr} and B_{cr} increases, the image quality decreases. Therefore, as a parameter to evaluate the image quality, the back-reflection suppression B_S is defined as

$$B_S = \frac{1 - B_{pr}}{1 + B_{cr}}. \quad (10)$$

B_S always has a value greater than or equal to zero and less than or equal to one because $B_{cr} \geq 0$ and $0 \leq B_{pr} \leq 1$. As in Eq. (10), when B_{pr} and B_{cr} decrease, B_S increases. Moreover, an increase in B_S means enhancement of back-reflection suppression and improvement of the image quality.

3.3. Optical efficiency

The optical efficiency indicates the efficiency of light transmission of an illumination system. This is the significant design factor for typical illumination systems because it is related to determining the number of

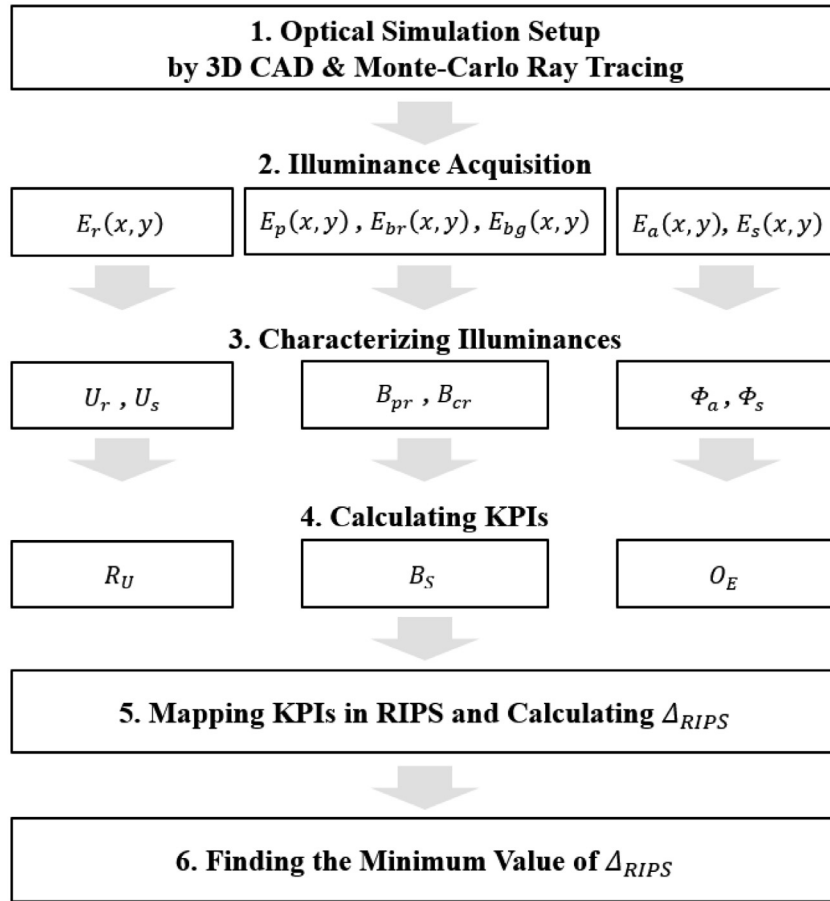


Fig. 4. Design procedure of the illumination system of the fundus camera.

light sources required and the power consumption. For SBFCs, optical efficiency is important to ensure a sufficient operating time even for a limited power source in a mobile device. Optical efficiency O_E is given by

$$O_E = \frac{\Phi_a}{\Phi_s}, \quad (11)$$

where Φ_a is the total luminous flux through the AA, and Φ_s is the total luminous flux emitted from the light sources. Φ_a and Φ_s can be calculated using the sum of illuminance and detector size by the defining the illuminance as follows:

$$\Phi_a = \frac{\iint_{A_a} E_a(x, y) dx dy}{A_a}, \quad (12)$$

$$\Phi_s = \frac{\iint_{A_s} E_s(x, y) dx dy}{A_s}, \quad (13)$$

where $E_a(x, y)$ and $E_s(x, y)$ are the illuminances of the AA and the LED light sources, respectively, and A_a and A_s are the areas of the detectors. Unless light comes from outside the device, O_E has a value of zero or more and one or less according to the law of conservation of energy.

4. Design of fundus camera illumination optics

4.1. Design procedure using KPIs

The design procedure for the fundus camera illumination system is illustrated in Fig. 4. KPIs, including R_U , B_S , and O_E , are calculated as described in Section 3 through the optical simulation for each design case. Subsequently, the KPIs are mapped into a normalized three-dimensional RIPS, and Δ_{RIPS} is calculated as the Euclidean distance between the

IDP and ADP in RIPS. The final design was obtained by determining the minimum of Δ_{RIPS} . Taguchi method and RSM were applied to determine the final design. Although neither Taguchi method nor RSM can guarantee a global optimum, both are practically useful for parameter optimization and have been widely used in various engineering fields [27–30].

In this study, two optical elements related to the SBFC illumination system, LED light source and AA, were considered while fixing the specifications of the HMP and OL. Five design variables that determine the structure and optical characteristics of the LED light source and AA were selected, as shown in Fig. 5. Two variables are related to the LEDs: the radius of the circle where the LEDs are arranged, LED_R , as shown in Fig. 5(a) and the distance between the bottom of the AA and the top of the PCB where the LEDs are attached, LED_H , as shown in Fig. 5(b). Three variables are related to the AA, as shown in Fig. 5(c): the scattering property of the AA surface in Gaussian distribution angle, AA_{HAZE} , and the outer and inner radii of the aperture area, AA_{RO} and AA_{RI} , respectively.

The sensitivities of the design variables were investigated using the Taguchi method, which helps to reduce the number of simulation experiments. Table 4 lists the design range and levels of the control factors, which are determined by considering the mechanical space constraints. These factors represent the design variables in the simulation experiment. The length and diameter of the OA handle, where the LED light source and AA are placed, are constrained for usability and portability. The available internal space is limited because the handle includes a battery unit.

The simulation experiments were designed using Minitab software version 20.3. An orthogonal array L27 was selected for five factors at three levels. An optical simulation was performed for each factor combination, and the number of tracing rays was 100 million.

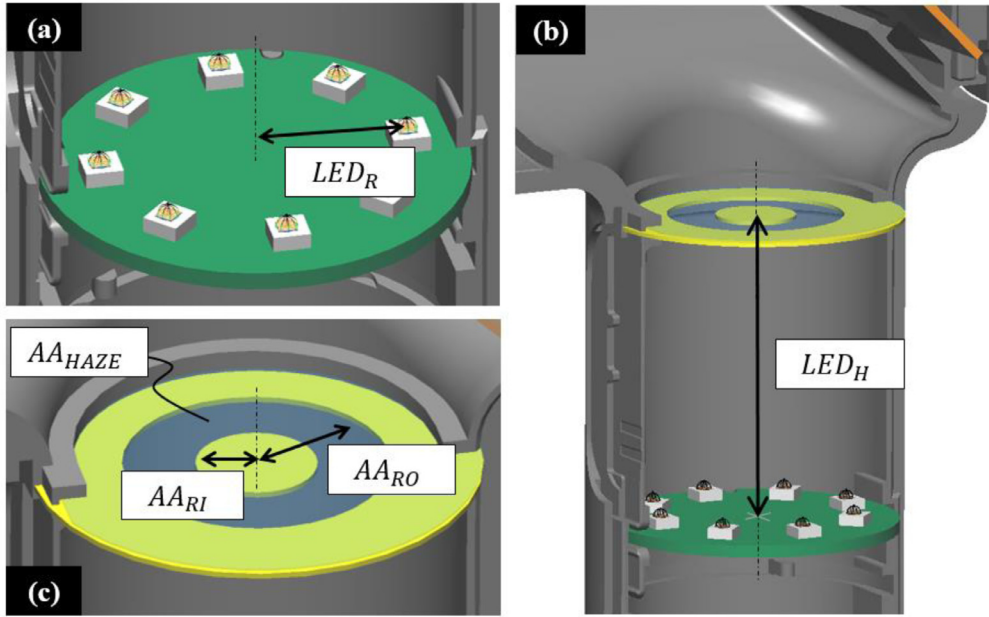


Fig. 5. Design variables that determine the structure and optical characteristics of the LED light source and AA; (a), (b) Two variables related to the LED light source; (c) Three variables related to AA.

Table 4
The design range and levels of control factors for the Taguchi method.

Control Factors	Unit	Level		
		Level 1	Level 2	Level 3
LED_R	mm	10	12	14
LED_H	mm	30	40	50
AA_{HAZE}	°	0	1	2
AA_{RO}	mm	12	14	16
AA_{RI}	mm	3	5	7

The KPIs were calculated using the simulation results and mapped into RIPS, a three-dimensional space with three independent coordinates consisting of the three KPIs: R_U , B_S , and O_E . In RIPS, the KPIs of the IDP are (1, 1, 1) because the KPIs were set to values between zero and one. The higher the KPI values, the better the performance. On the other hand, the KPIs of the ADPs correspond to (R_U, B_S, O_E) . To compare the performance of each ADP with that of the IDP, the Euclidean distance between them was quantified as Δ_{RIPS} , which is given by

$$\Delta_{RIPS} = \sqrt{(1 - R_U)^2 + (1 - B_S)^2 + (1 - O_E)^2}. \quad (14)$$

As Δ_{RIPS} decreases, which it means closer to IDP, the optical performance improves. The Δ_{RIPS} , including the IDP and 27 ADPs, created by the Taguchi method are shown in Fig. 6. The red dot represents the IDP, and the black dots indicate ADPs.

The Δ_{RIPS} calculated from the simulation result was converted into a signal-to-noise (S/N) ratio to measure the quality characteristics indicating the degree of deviation from the desired value [31]. Since our methodology aims to lower Δ_{RIPS} , the S/N ratio S/N for smaller-the-better quality characteristics was applied as [32]

$$S/N = -10 \log \left(\frac{1}{n} \sum_{i=1}^n y_i^2 \right), \quad (15)$$

where n is the number of simulation experiments, and y_i is the response (Δ_{RIPS}) for the i^{th} run. A larger S/N indicates a more desirable factor. The orthogonal arrays with the calculated KPIs, Δ_{RIPS} , and S/N for the ADPs are listed in Table 5.

The main effect plot of the mean of S/N with respect to the control factors is shown in Fig. 7, which shows that it is desirable to place LED_R , LED_H , and AA_{HAZE} on level 2 and AA_{RO} and AA_{RI} on level 1

to lower Δ_{RIPS} . The design values of LED_R , LED_H , AA_{HAZE} , AA_{RO} , and AA_{RI} were 12 mm, 40 mm, 1.0°, 12 mm, and 3 mm, respectively.

Response surface methodology (RSM) was performed for additional fine-tuning to obtain a smaller Δ_{RIPS} . RSM is a collection of mathematical and statistical techniques useful in modeling and analysis of problems in which the response of interest is influenced by several variables, and the objective is to optimize this response [33]. A central composite design (CCD) using a half-fraction factorial was applied to design simulation experiments for the five factors. Thirty-two simulation experiments were conducted, which included the center point and five replications at the center point, 16 corner points, and 10 star points. Parameter α , representing the distance from the center point to each star point, is determined as [34]

$$\alpha = \left[\frac{2^{k-f}(n_c)}{n_s} \right]^{1/4}, \quad (16)$$

where k is the number of factors, f is the level of fractionation in a two-level factorial design, and n_c and n_s are the numbers of replications at each corner and star point, respectively. In our case, we have $n_c = n_s = 1$, $k = 5$, and $f = 1$. Hence, $\alpha = 2$. Table 6 lists the design range and levels of the coded factors for the CCD-based RSM. Here, the central levels were determined based on the desirable variables obtained using the Taguchi method.

The full quadratic polynomial Y used as a mathematical model to approximate the relationship between the response and design variables is represented as [35]

$$Y = \beta_0 + \sum_{i=1}^k \beta_i X_i + \sum_{i=1}^k \beta_{ii} X_i^2 + \sum_{i \leq j}^k \sum_j^k \beta_{ij} X_i X_j + \epsilon, \quad (17)$$

where k is the number of factors, β_0 is the model constant, β_i are the coefficients of linear factors, β_{ij} and β_{ii} are the coefficients of the factors that interact with each other, ϵ is a statistical error, X_i and X_j are the factors. Minitab software version 20.3 was used to create the orthogonal arrays and to analyze and fit the data. An orthogonal array with the calculated KPIs and responses is presented in Table 7. The predicted value of Δ_{RIPS} , which is the response Y in Eq. (17), can be regressed in

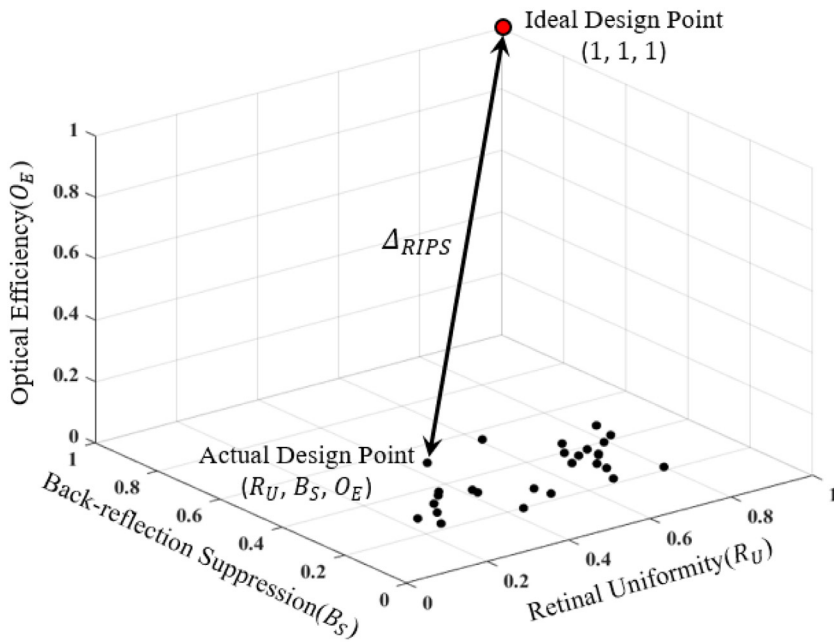


Fig. 6. Retinal illumination performance space (RIPS); The red dot represents the IDP, and the black dots indicate the ADPs. Δ_{RIPS} means the Euclidean distance between the IDP and an ADP.

Table 5

The orthogonal array with calculated KPIs, Δ_{RIPS} , and S/N .

Run No.	Control Factors in Levels					KPIs			Δ_{RIPS}	S/N
	LED_R	LED_H	AA_{HAZE}	AA_{RO}	AA_{RI}	R_U	B_S	O_E		
1	1	1	1	1	1	0.581	0.251	0.106	1.239	-1.861
2	1	1	1	1	2	0.645	0.225	0.092	1.246	-1.908
3	1	1	1	1	3	0.447	0.174	0.072	1.361	-2.675
4	1	2	2	2	1	0.644	0.260	0.091	1.225	-1.762
5	1	2	2	2	2	0.582	0.228	0.083	1.270	-2.074
6	1	2	2	2	3	0.166	0.181	0.070	1.494	-3.485
7	1	3	3	3	1	0.727	0.122	0.068	1.309	-2.339
8	1	3	3	3	2	0.615	0.138	0.062	1.331	-2.484
9	1	3	3	3	3	0.202	0.153	0.054	1.500	-3.522
10	2	1	2	3	1	0.678	0.229	0.140	1.199	-1.578
11	2	1	2	3	2	0.657	0.223	0.127	1.218	-1.712
12	2	1	2	3	3	0.625	0.199	0.108	1.256	-1.981
13	2	2	3	1	1	0.768	0.392	0.065	1.140	-1.137
14	2	2	3	1	2	0.662	0.364	0.056	1.187	-1.491
15	2	2	3	1	3	0.659	0.307	0.044	1.229	-1.791
16	2	3	1	2	1	0.642	0.226	0.061	1.268	-2.064
17	2	3	1	2	2	0.648	0.203	0.055	1.285	-2.178
18	2	3	1	2	3	0.483	0.166	0.047	1.368	-2.722
19	3	1	3	2	1	0.237	0.206	0.121	1.408	-2.974
20	3	1	3	2	2	0.235	0.205	0.110	1.418	-3.034
21	3	1	3	2	3	0.219	0.198	0.092	1.442	-3.177
22	3	2	1	3	1	0.328	0.217	0.090	1.376	-2.771
23	3	2	1	3	2	0.336	0.210	0.082	1.382	-2.808
24	3	2	1	3	3	0.217	0.185	0.070	1.464	-3.308
25	3	3	2	1	1	0.566	0.495	0.043	1.166	-1.335
26	3	3	2	1	2	0.406	0.463	0.038	1.252	-1.950
27	3	3	2	1	3	0.369	0.106	0.067	1.438	-3.154

Table 6

The design range and levels of coded factors for CCD-based RSM.

Variables	Unit	Levels (Coded Factors)				
		$-\alpha$ (-2)	Lower (-1)	Central (0)	Upper (+1)	$+\alpha$ (+2)
LED_R	mm	10	11	12	13	14
LED_H	mm	34	37	40	43	46
AA_{HAZE}	°	1.0	1.5	2.0	2.5	3.0
AA_{RO}	mm	10	11	12	13	14
AA_{RI}	mm	2.0	2.5	3.0	3.5	4.0

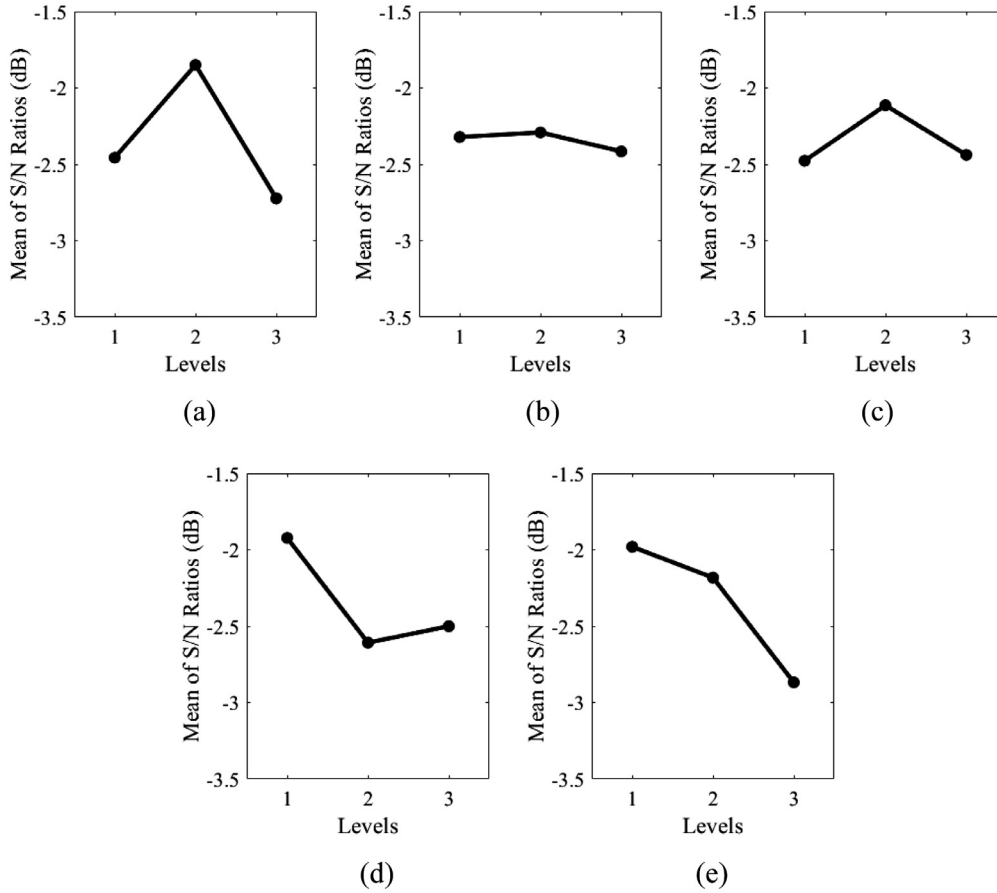


Fig 7. The main effect plot of the mean of S/N ; (a) LED_R , (b) LED_H , (c) AA_{HAZE} , (d) AA_{RO} , (e) AA_{RI} .

Table 7

The orthogonal array with the calculated KPIs and responses.

Run No.	Coded Factors					KPIs			Responses	
	LED_R	LED_H	AA_{HAZE}	AA_{RO}	AA_{RI}	R_U	B_S	O_E	Δ_{RIPS}	$\hat{\Delta}_{RIPS}$
1	0	-2	0	0	0	0.733	0.358	0.083	1.151	1.157
2	-1	+1	+1	+1	-1	0.725	0.272	0.070	1.212	1.210
3	-1	+1	+1	-1	+1	0.632	0.262	0.048	1.259	1.257
4	+1	-1	-1	-1	-1	0.476	0.471	0.061	1.199	1.191
5	0	0	0	0	0	0.768	0.392	0.065	1.140	1.137
6	0	0	+2	0	0	0.728	0.347	0.065	1.173	1.177
7	0	0	0	-2	0	0.527	0.457	0.044	1.197	1.210
8	+1	-1	+1	+1	-1	0.638	0.374	0.085	1.167	1.164
9	0	0	0	0	0	0.768	0.392	0.065	1.140	1.137
10	0	0	0	0	-2	0.783	0.397	0.067	1.132	1.145
11	+1	+1	+1	+1	+1	0.648	0.384	0.065	1.174	1.174
12	0	+2	0	0	0	0.757	0.353	0.052	1.173	1.181
13	+2	0	0	0	0	0.457	0.491	0.061	1.198	1.206
14	+1	+1	-1	+1	-1	0.659	0.375	0.067	1.174	1.169
15	+1	-1	+1	-1	+1	0.482	0.469	0.057	1.199	1.196
16	0	0	0	0	0	0.768	0.392	0.065	1.140	1.137
17	-1	+1	-1	-1	-1	0.666	0.307	0.050	1.222	1.215
18	0	0	0	+2	0	0.738	0.301	0.087	1.179	1.180
19	0	0	-2	0	0	0.747	0.349	0.065	1.167	1.177
20	0	0	0	0	0	0.768	0.392	0.065	1.140	1.137
21	-2	0	0	0	0	0.701	0.233	0.068	1.244	1.250
22	0	0	0	0	+2	0.717	0.381	0.061	1.160	1.161
23	-1	-1	-1	+1	-1	0.643	0.292	0.089	1.207	1.203
24	+1	+1	+1	-1	-1	0.546	0.409	0.048	1.209	1.203
25	+1	+1	-1	-1	+1	0.513	0.484	0.046	1.190	1.185
26	-1	-1	+1	-1	-1	0.674	0.341	0.065	1.190	1.184
27	-1	+1	-1	+1	+1	0.713	0.287	0.067	1.209	1.207
28	0	0	0	0	0	0.768	0.392	0.065	1.140	1.137
29	+1	-1	-1	+1	+1	0.593	0.341	0.081	1.202	1.201
30	-1	-1	+1	+1	+1	0.729	0.297	0.086	1.185	1.185
31	-1	-1	-1	-1	+1	0.652	0.334	0.061	1.203	1.199
32	0	0	0	0	0	0.768	0.392	0.065	1.140	1.137

Table 8
Comparison results between the predicted and the simulated Δ_{RIPS} .

Design Variables			KPIs				Responses		
LED_R	LED_H	AA_{HAZE}	AA_{RO}	AA_{RI}	R_U	B_S	O_E	$\hat{\Delta}_{RIPS}$	Δ_{RIPS}
12.4	37.0	2.0	12.4	2.4	0.759	0.389	0.077	1.137	1.133

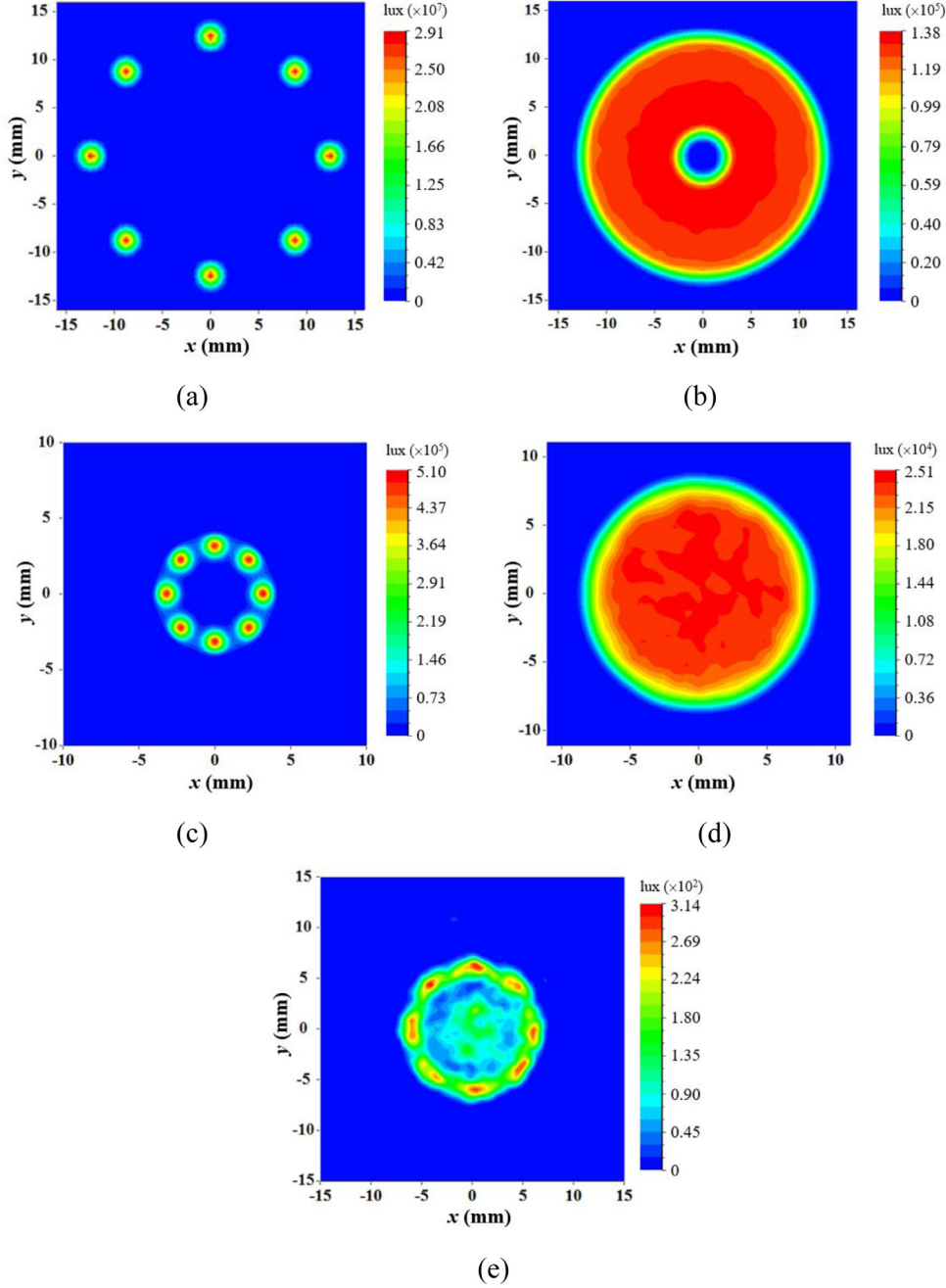


Fig. 8. Simulated illuminance on each detector of the determined design; (a) $E_s(x, y)$ at the LEDs, (b) $E_a(x, y)$ at the AA, (c) $E_p(x, y)$ on the pupil plane, (d) $E_r(x, y)$ on the retina, and (e) $E_{br}(x, y)$ on the image sensor.

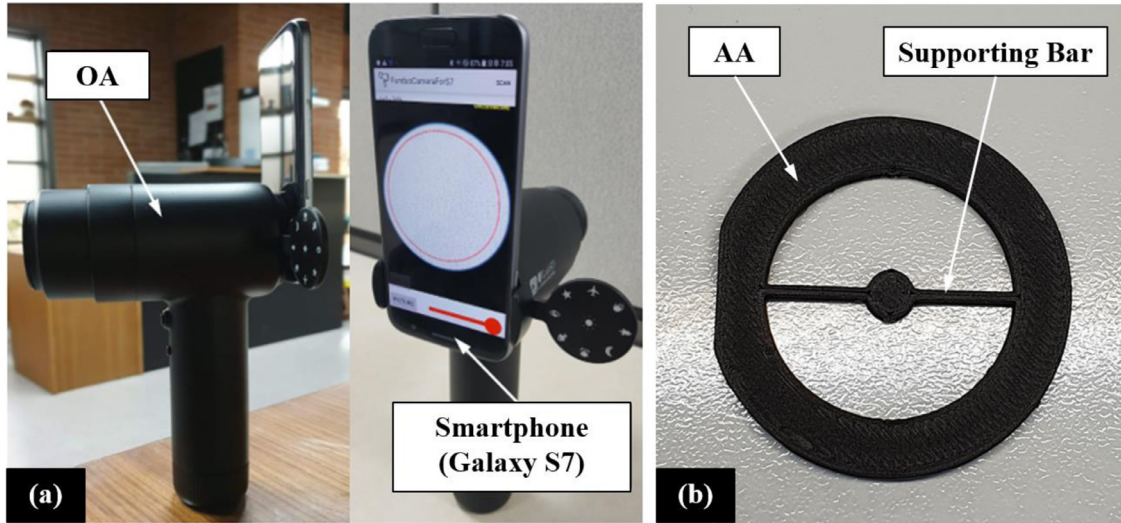


Fig. 9. (a) Working prototype built with the obtained design variables. The OA was assembled with the smartphone, Samsung Galaxy S7; (b) The AA mounted inside the OA was manufactured by 3D printing with black polymer material. The inner circle of the AA is fixed by supporting bars linked with the outer ring.

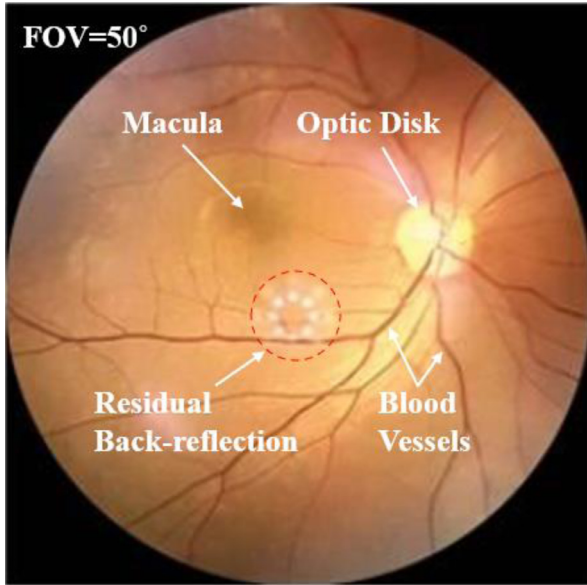


Fig. 10. Fundus image of a male in his 40 s with the normal eyes obtained with the fabricated working prototype.

a coded form as

$$\begin{aligned} \hat{\Delta}_{RIPS} = & 1.1374 - 0.0111 LED_R + 0.0060 LED_H \\ & + 0.0001 AA_{HAZE} - 0.0074 AA_{RO} + 0.0041 AA_{RI} + \\ & 0.0227 LED_R^2 + 0.0080 LED_H^2 + 0.0100 AA_{HAZE}^2 \\ & + 0.0144 AA_{RO}^2 + 0.0039 AA_{RI}^2 - \\ & 0.0087 LED_R LED_H - 0.0013 LED_R AA_{HAZE} \\ & - 0.0012 LED_R AA_{RO} - 0.0004 LED_R AA_{RI} + \\ & 0.0082 LED_H AA_{HAZE} - 0.0051 LED_H AA_{RO} \\ & - 0.0008 LED_H AA_{RI} - 0.0061 AA_{HAZE} AA_{RO} + \\ & 0.0025 AA_{HAZE} AA_{RI} - 0.0014 AA_{RO} AA_{RI}, \end{aligned} \quad (18)$$

where $\hat{\Delta}_{RIPS}$ is the predicted Δ_{RIPS} . The coefficient of determination R^2 , which measures how well the data fit the regression model, was

0.969, and the adjusted R^2 is 0.912. A high R^2 indicates that the predicted values are expected to explain the simulated values well.

From Eq. (18), the minimum $\hat{\Delta}_{RIPS}$ was determined to be 1.137 by solving the equation using the software. For the determined design, the design values for LED_R , LED_H , AA_{HAZE} , AA_{RO} , and AA_{RI} are 12.4 mm, 37.7 mm, 2.3°, 12.4 mm, and 2.4 mm, respectively. With the design values, a simulation to obtain illuminance distributions were performed using LightTools. Fig. 8 shows the simulated illuminance for each detector in the determined design. As shown in Fig. 8(a), eight LEDs were separately observed for $E_s(x, y)$. The peak illumination appears 12.4 mm away from the center of the array, which is identical to the LED_R of the determined design. Fig. 8(b) shows the illuminance at AA, $E_a(x, y)$. The designated shape of the AA blocks the ray toward the center. In $E_p(x, y)$ on the pupil plane, as shown in Fig. 8(c), the ray through the center area of the pupil was suppressed effectively to avoid back-reflection by the cornea. Fig. 8(d) shows the illuminance on the retina, $E_r(x, y)$, and the rays are uniformly illuminated in the whole area of the retina. As shown in Fig. 8(e), several hot spots were observed in $E_{br}(x, y)$ in the image sensor, indicating that back-reflection was not completely eliminated. However, it is challenging to eliminate back-reflection in a simple illumination system as in SBFC, and the degree of back-reflection shown in Fig. 8(e) was regarded as practically acceptable; therefore, a clinical test using a working prototype was conducted, as described in Section 4.2.

Individual KPIs were calculated from the simulated illuminance, and the R_U , B_S , and O_E values were 0.759, 0.389, and 0.077, respectively. Moreover, Δ_{RIPS} was calculated using the KPIs, and the result was 1.133. The predicted and simulated Δ_{RIPS} values are compared in Table 8. The difference between these values is negligible. Although not covered in this study, improved results can be obtained by applying independent weights to each KPI during the design process.

4.2. Prototyping and clinical test

A working prototype was constructed using the determined design variables, as shown in Fig. 9(a). The fabricated OA was assembled with the smartphone, Samsung Galaxy S7, as an out-of-season smartphone model that can be easily obtained in third countries. Fig. 9(b) shows the AA mounted inside the OA. AA was manufactured by 3D printing using black polymer material. The inner circle of the AA was fixed using supporting bars linked to the outer ring.

Clinical tests were conducted with the working prototype. Ethical approval for the study was obtained from the Yonsei University Insti-

tutional Review Board (IRB ID: 4–2021–0498). The subject was a male in his 40 s with normal eyes, and the fundus was examined with the pupil dilated using a mydriatic agent. Fig. 10 shows the fundus image obtained using the fabricated working prototype. The image having approximately 50° of FOV can be acquired in one shot. This implies that the developed illumination system effectively illuminated an area corresponding to the FOV of the camera. The macula in the upper left of the image, optic disk in the upper right, and blood vessels spread throughout the eye were observed. The proposed design process considered minimizing back-reflection, but a slight residual back-reflection was observed in the center of the fundus image obtained by the working prototype, as shown in Fig. 10. To suppress the residual back-reflection, Köhler illumination or a similar optical system can be employed as mentioned in Introduction. However, since our design philosophy focuses on simplicity and the minimization of optical structures, it is not appropriate to introduce such solutions that require complex optics. And as a result of discussions with ophthalmologists on the effect of residual back-reflection of the fundus image on diagnosis, capillaries, fovea centralis, and optic disk were clearly observed through the image, so even if there is some residual back-reflection, it can be sufficiently utilized for clinical diagnosis for screening tests. While the current prototype is useful for clinical purposes, additional ways to incorporate image processing techniques, such as machine learning-based algorithms that can reduce residual back-reflection and improve medical image quality without optical additions, could be explored [36–38]. Furthermore, this paper achieved cost reduction and compactness of the illumination system by utilizing the conventional smartphones and the OA including imaging optics, as shown in Figs. 1 and 2. For further miniaturization of the optical system, the possibility of introducing smaller and thinner imaging optics into the OA can be considered as a future study. To achieve this while maintaining the advantages of a compact and portable SBFC, there is a need to use novel optical components such as meta-lenses [39,40], tunable liquid crystal lenses [41], and tunable gradient index lenses [42], which are much more compact than conventional imaging components such as refractive lenses.

5. Conclusions

This study introduced a novel illumination design methodology to obtain high-quality fundus images of SBFCs. The KPIs using the characterized illuminances, R_U , B_S , and O_E , are defined for the illumination system. Each KPI was mapped into the RIPS, in which the KPIs were combined into a single parameter, Δ_{RIPS} , the quantitative difference evaluated as the Euclidean distance between the IDP and ADP. A compact SBFC illumination system was designed with five variables to verify the methodology. A lower Δ_{RIPS} corresponding to a higher illumination performance was determined using the Taguchi method and RSM. The determined design values for LED_R , LED_H , AA_{HAZE} , AA_{RO} , and AA_{RI} are 12.4 mm, 37.7 mm, 2.3°, 12.4 mm, and 2.4 mm, respectively. In the design, the R_U , B_S , and O_E were 0.759, 0.389, and 0.077, respectively, and Δ_{RIPS} was 1.113. Finally, a working prototype was built, and the fundus image of a male in his 40 s with normal eyes was acquired by clinical testing. The blood vessels, optic nerve, and macula were observed at high resolution. The image quality of the manufactured device was assessed by ophthalmologists at Yonsei Severance Hospital as the highest level among existing SBFCs. In addition to fundus cameras, various studies have been conducted on medical diagnostic devices using smartphones. Our research can be applied universally to the design of smartphone-based diagnostic devices, including multiple light source illumination systems, contributing to improving design performance.

Declaration of Competing Interest

The authors declare the following financial interests/personal relationships which may be considered as potential competing interests:

No-Cheol Park reports financial support was provided by Samsung Electronics Co., Ltd. Seung-Jae Lee reports a relationship with Samsung Electronics Co., Ltd. that includes: employment. Seung-Jae Lee has patent #P2020–0,001,738 (Korea) pending to Samsung Electronics. Kyung-Mo Yang and Keun-Bum Lee are currently employed in Samsung Electronics.

CRedit authorship contribution statement

Seung-Jae Lee: Conceptualization, Methodology, Validation, Formal analysis, Writing – original draft. **Kyung-Mo Yang:** Conceptualization, Investigation, Funding acquisition. **Keun-Bum Lee:** Investigation, Validation. **No-Cheol Park:** Writing – review & editing, Supervision.

Data availability

Data will be made available on request.

Acknowledgement

This work was supported by Samsung Electronics, Co., Ltd. in Suwon, South Korea.

References

- [1] Abràmoff MD, Garvin MK, Sonka M. Retinal imaging and image analysis. *IEEE Rev Biomed Eng* 2010;3:169–208. doi:10.1109/RBME.2010.2084567.
- [2] WHO (World Health Organization). World report on. Vision. 2019.
- [3] Panwar N, Huang P, Lee J, Keane PA, Chuan TS, Richhariya A, et al. Fundus photography in the 21st century — a review of recent technological advances and their implications for worldwide healthcare. *Telemed J E Health* 2016;22:198–208. doi:10.1089/tmj.2015.0068.
- [4] Chalam KV, Brar VS, Keshavamurthy R. Evaluation of modified portable digital camera for screening of diabetic retinopathy. *Ophthalmic Res* 2009;42:60–2. doi:10.1159/000219687.
- [5] Tran K, Mendel TA, Holbrook KL, Yates PA. Construction of an inexpensive, handheld fundus camera through modification of a consumer “point-and-shoot” camera. *Invest Ophthalmol Vis Sci* 2012;53:7600–7. doi:10.1167/iops.12.10449.
- [6] Haddock LJ, Kim DY, Mukai S. Simple, inexpensive technique for high-quality smartphone fundus photography in human and animal eyes. *J Ophthalmol* 2013;2013:518479. doi:10.1155/2013/518479.
- [7] Myung D, Jais A, He L, Blumenkranz MS, Chang RT. 3D printed smartphone indirect lens adapter for rapid, high quality retinal imaging. *J MTM* 2014;3:9–15. doi:10.7309/jmtm.3.1.3.
- [8] Russo A, Morescalchi F, Costagliola C, Delcassi L, Semeraro F. A novel device to exploit the smartphone camera for fundus photography. *J Ophthalmol* 2015;2015:823139. doi:10.1155/2015/823139.
- [9] Toslak D, Ayata A, Liu C, Erol MK, Yao X. Wide-field smartphone fundus video camera based on miniaturized indirect ophthalmoscopy. *Retina* 2018;38:438–41. doi:10.1097/IAE.0000000000001888.
- [10] Shanmugam MP, Mishra DK, Madhukumar R, Ramanjulu R, Reddy SY, Rodrigues G. Fundus imaging with a mobile phone: a review of techniques. *Indian J Ophthalmol* 2014;62:960–2. doi:10.4103/0301-4738.143949.
- [11] Wintergerst MWM, Petrak M, Li JQ, Larsen PP, Berger M, Holz FG, et al. Non-contact smartphone-based fundus imaging compared to conventional fundus imaging: a low-cost alternative for retinopathy of prematurity screening and documentation. *Sci Rep* 2019;9:19711. doi:10.1038/s41598-019-56155-x.
- [12] Thomas SA, et al. Design of a portable retinal imaging module with automatic abnormality detection. *Biomed Signal Process Control* 2020;60 10.1962(2020).
- [13] Witmer MT, Kiss S. Wide-field imaging of the retina. *Surv Ophthalmol* 2013;58:143–54. doi:10.1016/j.survophthal.2012.07.003.
- [14] Xing C, Xu F, Lu F, Tian G, Shang M. Design of portable fundus camera system based on mobile phone. In: *Proceedings of the SPIE 10839, 9th international symposium on advanced optical manufacturing and testing technologies: optical test, measurement technology, and equipment*; 2019. 108391K. doi:10.1117/12.2506700.
- [15] DeHoog E, Schwiegerling J. Optimal parameters for retinal illumination and imaging in fundus cameras. *Appl Opt* 2008;47:6769–77. doi:10.1364/ao.47.006769.
- [16] Ma C, Cheng D, Xu C, Wang Y. Design, simulation and experimental analysis of an anti-stray-light illumination system of fundus camera. In: *Proceedings of the SPIE 9272, optical design and testing VI*; 2014. 92720H. doi:10.1117/12.2073619.
- [17] LightTools tutorial, backlight design and analysis in LightTools, Slide 36. Synopsis. 2008.
- [18] LightTools version 8.5, Synopsis. <https://www.synopsys.com/optical-solutions/lighttools.html>, 2023.
- [19] Hopkins R.E., Hanau R. Chapter 4, US Defense Supply Agency. Washington, DC. In: *Military standardization handbook—Optical design (MIL-HDBK-141)*; 1962.
- [20] DeHoog E, Schwiegerling J. Fundus camera systems: a comparative analysis. *Appl Opt* 2009;48:221–8. doi:10.1364/ao.48.000221.
- [21] ISO 10940: 2009. Ophthalmic instruments - Fundus cameras. International Organization for Standardization.

- [22] Moreno I. Illumination uniformity assessment based on human vision. *Opt Lett* 2010;35:4030–2. doi:[10.1364/OL.35.004030](https://doi.org/10.1364/OL.35.004030).
- [23] Mori Y, Tanahashi K, Tsuji S. Quantitative evaluation of "mura" in liquid crystal displays. *Opt Eng* 2004;43(11). doi:[10.1117/1.1768942](https://doi.org/10.1117/1.1768942).
- [24] Liou HL, Brennan NA. Anatomically accurate, finite model eye for optical modeling. *J Opt Soc Am A Opt Image Sci Vis* 1997;14:1684–95. doi:[10.1364/josaa.14.001684](https://doi.org/10.1364/josaa.14.001684).
- [25] ISO 9241-302. Ergonomics of human-system interaction - Part 302 Terminology for electronic visual displays. International Organization for Standardization; 2008.
- [26] Wüller D, Gabele H. The usage of digital cameras as luminance meters. *SPIE Digit Photogr III Vol* 2007;6502. doi:[10.1117/12.703205](https://doi.org/10.1117/12.703205).
- [27] Yeh CH, Han P, Wang LJ, Lin En-T. Using design of experiment for parameter optimization on smart headlamp optics design. *Appl Opt* 2019;58:7661–83. doi:[10.1364/AO.58.007661](https://doi.org/10.1364/AO.58.007661).
- [28] He J, Li G, Zhou R, Wang Q. Optimization of permanent-magnet spherical motor based on taguchi method. *IEEE Trans Magn* 2020;56:8200107. doi:[10.1109/TMAG.2019.2947863](https://doi.org/10.1109/TMAG.2019.2947863).
- [29] Chelladurai SJS, Murugan K, Ray AP, Upadhyaya M, Narasimharaj V, Gnanasekaran S. Optimization of process parameters using response surface methodology: a review. *Mater Today Proc* 2021;37:1301–4. doi:[10.1016/j.matpr.2020.06.466](https://doi.org/10.1016/j.matpr.2020.06.466).
- [30] Gabriella Dellino A, Kleijnen JPC, Meloni C. Robust optimization in simulation: taguchi and Response Surface Methodology. *Int J Prod Econ* 2010;125:52–9. doi:[10.1016/j.ijpe.2009.12.003](https://doi.org/10.1016/j.ijpe.2009.12.003).
- [31] Yang WH, Tarn YS. Design optimization of cutting parameters for turning operations based on the Taguchi method. *J Mater Process Technol* 1998;84:122–9. doi:[10.1016/S0924-0136\(98\)00079-X](https://doi.org/10.1016/S0924-0136(98)00079-X).
- [32] Asghar A, Abdul Raman AA, Daud WM. A comparison of central composite design and Taguchi method for optimizing Fenton process. *Sci World J* 2014;2014:869120. doi:[10.1155/2014/869120](https://doi.org/10.1155/2014/869120).
- [33] Montgomery DC. Design and analysis of experiments. John Wiley & Sons; 2012. p. 478. Page.
- [34] Kutner MH, Nachtsheim CJ, Neter J, Li W. Applied linear statistical models. 5th ed. McGraw-Hill; 2005.
- [35] Shojaei S, Band SS, Farizhandi AAK, Ghoroqi M, Mosavi A. Application of Taguchi method and response surface methodology into the removal of malachite green and auramine-O by NaX nanozeolites. *Sci Rep* 2021;11:16054. doi:[10.1038/s41598-021-95649-5](https://doi.org/10.1038/s41598-021-95649-5).
- [36] Palmer DW, Coppin T, Rana K, Dansereau DG, Suheimat M, Maynard M, et al. Glare-free retinal imaging using a portable light field fundus camera. *Biomed Opt Express* 2018;9:3178–92. doi:[10.1364/BOE.9.003178](https://doi.org/10.1364/BOE.9.003178).
- [37] Amanlou A, Suratgar AA, Tavoosi J, Mohammadzadeh A, Mosavi A. Single-image reflection removal using deep learning: a systematic review. *IEEE Access* 2022;10:29937–53. doi:[10.1109/ACCESS.2022.3156273](https://doi.org/10.1109/ACCESS.2022.3156273).
- [38] Chao N, Chao X, Bo F, Yue C. Specular reflections removal for endoscopic images based on improved criminisi algorithm. In: Proceedings of the IEEE 6th international conference on computer and communication systems (ICCCS); 2021. p. 291–6. doi:[10.1109/ICCCS52626.2021.9449139](https://doi.org/10.1109/ICCCS52626.2021.9449139).
- [39] Chen M, Yan Y, Liu X, Wu Y, Zhang J, Yuan J, et al. Edge detection with meta-lens: from one dimension to three dimensions. *Nanophotonics* 2021;10:3709–15. doi:[10.1515/nanoph-2021-0239](https://doi.org/10.1515/nanoph-2021-0239).
- [40] Chen M, Liu X, Wu Y, Zhang J, Yuan J, Zhang Z, et al. A meta-device for intelligent depth perception. *Adv Mater* 2022;2107465. doi:[10.1002/adma.202107465](https://doi.org/10.1002/adma.202107465).
- [41] Kumar MB, Kang D, Jung J, Park H, Hahn J, Choi M, et al. Compact vari-focal augmented reality display based on ultrathin, polarization-insensitive, and adaptive liquid crystal lens. *Opt Lasers Eng* 2020;128:106006. doi:[10.1016/j.optlaseng.2020.106006](https://doi.org/10.1016/j.optlaseng.2020.106006).
- [42] Guo Z, Li G, Chen SL. Miniature probe for all-optical double gradient-index lenses photoacoustic microscopy. *J Biophotonics* 2018;11:e201800147. doi:[10.1002/jbio.201800147](https://doi.org/10.1002/jbio.201800147).



Seung-Jae Lee received B.S. degree in Dept. of Mechanical Engineering from Sogang University in 2002 and M.S degree in Information Storage Engineering from Yonsei University in 2004. Mr. Lee is currently a Ph.D. candidate at Dept. of Mechanical Engineering in Yonsei University, and working for Samsung Electronics. His-research interest is in optical and optomechanical design for illumination systems.



Kyung-Mo Yang received B.S. degree in Dept. of Mechanical Engineering from Hanyang University in 2006. Mr. Yang is currently in charge of the Circular Economy Lab in Samsung Electronics and working on a strategic plan for materials and products. Mr. Yang is also a leader of Galaxy Upcycling project. He is discovering and operating various projects that can utilize used-Galaxy valuably for new purposes.



Keun-Bum Lee received B.S. degree in Dept. of Mechanical Engineering from Chungbuk National University in 2010. Mr. Lee is currently working for Samsung Electronics. His-research interest is in illumination design for home appliances and IT devices using optical simulation and analysis.



No-Cheol Park received a B.S., M.S., and Ph.D. degree in Dept. of Mechanical Engineering from Yonsei University in 1986, 1988 and 1997 respectively. He is currently working in Yonsei University as a professor of the Mechanical Engineering. His-research interests include the mechanical vibration and optomechanics system.